

Experimental evaluation of fluid connectivity in two-phase flow in porous media

Samaneh Vahid Dastjerdi^{a,c,*}, Nikolaos Karadimitriou^{a,c}, S. Majid Hassanizadeh^{b,c},
Holger Steeb^{a,c}

^a Institute for Applied Mechanics (CE), University of Stuttgart, Pfaffenwaldring 7, Stuttgart, 70569, Germany

^b Department of Earth Sciences, Utrecht University, Princetonlaan 8a, Utrecht, 3584 CB, Netherlands

^c SC SimTech, University of Stuttgart, Pfaffenwaldring 5, Stuttgart, 70569, Germany

ARTICLE INFO

Keywords:

Microfluidic experiments
Two-phase flow
Phase percolation
Interfacial area
Image processing
Optical microscopy

ABSTRACT

In this work, we provide a physically-consistent modeling approach for two-phase porous media flow, by including percolating interfacial area and saturation as state variables. For this purpose, we combine two continuum theories for two-phase flow which have been individually proven to be conditionally valid. This means the potential use of the connected-to-the-flow interfacial area as a state variable is tested utilizing time-resolved microfluidic experiments, for various flux boundary conditions. Moreover, we observe and study a linear relation between the percolating saturation and interfacial area, which is persistent for the tested boundary conditions. In our microfluidic experiments, we employ optical microscopy to perform cyclic immiscible displacement experiments. Our results show that a continuum model, where capillary pressure, saturation, and specific interfacial area of the clusters connected to the flow are considered, is closer to a universal description of two-phase flow than the common approaches, where the only state variable is saturation.

1. Introduction

Defining the physical properties of a multi-phase displacement process in a porous medium is a fundamental prerequisite in many porous media fluid flow applications. Such applications include, but are not limited to, many natural phenomena, such as water infiltration (Parr and Bertrand, 1960; Lipiec et al., 2006), or saline water intrusion (Todd, 1974; Choudhury et al., 2001), and those of industrial interest. These include enhanced oil recovery (EOR) (Muggeridge et al., 2014; Alvarado and Manrique, 2010), or fuel cells (Abdelkareem et al., 2021; Sharaf and Orhan, 2014), among others. However, the theoretical frameworks under which the underlying physical processes are attempted to be described and modeled have been efficient to a specific extent, with the overall image still incomplete. The empirical closure equations in common continuum theories such as Leverett (1941), Brooks and Corey (1964), Land (1968) or Van Genuchten (1980), include saturation or effective/residual (trapped) saturation, as the only state variable. For example, Land (1968) obtains expressions for trapped and mobile non-wetting saturation and shows that they can be used in the calculation of wet-rock/fluid properties, such as relative permeability. In these approaches, the equations for saturation vs. capillary pressure must have different coefficients for different

displacement events to capture the history-dependent characteristics of two-phase flow in porous media.

Given that the aforementioned macroscale, i.e. continuum, approaches are case- and history-dependent, substantial theoretical, numerical, and experimental efforts have been made to come up with more physically-based and representative modeling approaches. These efforts mostly involve adding state variables other than saturation to the continuum-scale models. Among the list of proposed new state variables are: The area of the interfaces between the phases (Hassanizadeh and Gray, 1990, 1993), a topological measure known as Euler characteristic number (Herring et al., 2013; Schlüter et al., 2016; Miller et al., 2019; McClure et al., 2020), and connection of the phases to the flow path (Hilfer, 2006a,b; Armstrong et al., 2012; Herring et al., 2017). Moreover, several researchers identify and include more than one state variable at once (Osei-Bonsu et al., 2020; Vahid Dastjerdi et al., 2022a). For example Osei-Bonsu et al. (2020), have experimentally shown that parameters such as the Euler characteristic number, the percolating volume fraction of the fluids, and the fraction of the wetted solid surface, are adequate to describe the phases' state in their microfluidic experiments. These parameters have been shown to provide practical solutions towards making reservoir simulations more

* Corresponding author at: Institute for Applied Mechanics (CE), University of Stuttgart, Pfaffenwaldring 7, Stuttgart, 70569, Germany.

E-mail address: samaneh.vahiddastjerdi@mechbau.uni-stuttgart.de (S. Vahid Dastjerdi).

efficient (Khorsandi et al., 2021). However, a practical approach based on continuum theories and their applications are yet to be identified.

In this study, we are focusing on the approaches of Hassanizadeh and Gray (1990, 1993), who introduce specific interfacial area as a separate state variable, and Hilfer (2006a,b), where percolating and non-percolating volume fractions for each fluid phase are included. As one can see, the additional state variables in these two approaches are conceptually different. In Hassanizadeh–Gray’s approach, a new measure that accounts for the existence of interfaces is introduced. Hilfer’s approach focuses on the connectivity of fluid phases and still works with the traditional volumetric measure, namely saturation. Thus, they take different phenomena in multi-phase flow into account and can, potentially, be complementary. We hypothesize that their combination can improve our description of multi-phase flow in porous media.

Hilfer points out challenges, such as the inclusion of hysteresis and multivaluedness, mirroring the dynamic effects in a process, and the association of pore-scale parameters with macroscale averages as the reasons behind the inefficiency of the common macroscopic theories. He tries to overcome them by obtaining the capillary pressure function as an outcome of his theoretical framework, and not as an input. In this context, he considers residual saturation as non-percolating saturation, which depends on the process and the initial/boundary conditions. He also differentiates between percolating and non-percolating saturation in general. In other words, he introduces four saturation fields: percolating and non-percolating fractions of wetting and non-wetting saturations, instead of only wetting and non-wetting. A few numerical and experimental investigations have shown the potential of this theory (Hilfer and Doster, 2010; Doster and Hilfer, 2014; Hilfer et al., 2015). However, the extent of its validity under non-equilibrium conditions has not been shown yet.

In the extended continuum-mixture theory for porous media, developed by Hassanizadeh and Gray (1990, 1993), balance equations are developed for bulk phases, for interfaces, and for exchange processes over interfaces. Compared to classical continuum-scale theories of porous media, the interfaces (per unit volume) between the three phases (wetting, non-wetting, and solid), as the locus of any potential phase energy exchange, complement classical bulk state variables. Through safe assumptions for the fluid–solid interfaces, they reduce the essential state variables in their continuum theory to saturation and fluid–fluid specific interfacial area. Many numerical and experimental investigations have shown that including this extra state variable improves the modeling of the apparent hysteresis in quasi-static displacement events (Held and Celia, 2001; Cheng et al., 2004; Joekear-Niasar et al., 2008; Niessner and Hassanizadeh, 2008; Porter et al., 2009; Zhuang et al., 2017). However, the validity of this approach under transient flow conditions and for a wide range of capillary numbers has been questioned (Joekear-Niasar and Hassanizadeh, 2011; Shokri et al., 2022). For example, Karadimitriou et al. (2014) investigate the theory under transient conditions experimentally, with the use of microfluidics and direct, real-time visualization. They show that the inclusion of the specific interfacial area between the two fluids can improve the hysteretic behavior during cyclic drainage and imbibition events. They show capillary pressure–saturation–specific interfacial area creates a unique surface under given boundary conditions. However, different surfaces for different boundary conditions are needed. This raises the question of whether another state variable, in addition to specific interfacial area, is needed to account for the effective complex pore-scale fluid configurations on the macroscale.

Motivated by the results of Karadimitriou et al. (2014) and inspired by the theoretical approach of Hilfer (2006a,b), Vahid Dastjerdi et al. (2022a) perform a set of two-phase displacement experiments to investigate the role of disconnections in the evolution of the flow. They follow the extended continuum theory for two-phase flow, where specific interfacial area between the wetting and the non-wetting phase is brought into the constitutive equations. Their experiments include flow-controlled cyclic drainage and imbibition with three orders of

magnitude variation in the volumetric fluxes and the corresponding Ca number (10^{-7} to 10^{-5}). They conclude that considering both interfacial area and percolating saturation of the invading phase in two-phase porous media flow models can model the apparent hysteresis more efficiently. This signifies that describing two-phase flow with a single model is more feasible when both percolating saturation and interfacial area are considered as state variables.

However, in their experiments, the microfluidic cell they use facilitates strong corner/film flow, by construction. The extent of the corner/film flow is not observable and quantifiable with their experimental procedure and, therefore a reliable saturation for the connected wetting phase is not measurable. Thus, they only resolve the drainage events in terms of saturation, capillary pressure, and specific interfacial area between the wetting and the non-wetting phase during the flow, both on the micro- and macro-scale. They imply that further studying of imbibition processes needs to be carried out in a microfluidic cell with very well-defined connectivity of the wetting phase. The cell should also allow for the precise calculation of the wetting phase saturation, since the shadow (caused by curved channel walls) in glass microfluidic cells, prevents the wetting phase occupancy from being captured. Thus, the most feasible solution, to take their investigations further, is a microfluidic cell in which the permeability of the corners and the extent of films of the wetting phase is negligible.

Taking advantage of the capabilities of soft lithography (Xia and Whitesides, 1998; Karadimitriou et al., 2013) and optical microscopy (Karadimitriou et al., 2013), in the current contribution, we are presenting a set of microfluidic experiments in a porous domain made of Poly-Di-Methyl-Siloxane (PDMS). The primary motivation behind these experiments is to investigate our hypothesis during imbibition while excluding the corner/film flow effect for the wetting phase. The structure of the pores of the PDMS microfluidic cells, along with PDMS wetting properties, prohibits the pronounced connection between the wetting clusters and allows us to define connectivity reliably from the images and address the imbibition processes as well. However, by shifting to PDMS micromodels, other aspects of the experiments are also changed and included. For instance, the geometry of the porous domain is slightly different in the PDMS microfluidic cell in comparison to the glass micromodel used in Vahid Dastjerdi et al. (2022a). The pore throat/pore depth ratio in the PDMS cells differs from this in the glass microfluidic cells. Thus, the corresponding entry capillary pressure for the same planar location is different in the two cells. Moreover, due to the different manufacturing procedures, the channel shapes differ. The curved walls in the glass cell are replaced with almost perfect rectangular channels, in cross-section, in the PDMS microfluidic cell.

Another aspect that is different in these experiments is the wetting properties of the employed fluid–solid–fluid system. A concept known as Lenormand’s phase diagram (Lenormand et al., 1988) should be mentioned to elaborate further on this matter. Lenormand et al. (1988) perform drainage experiments with various viscosity ratios (M) between the non-wetting phase (as the invading fluid) and the wetting phase (as the defending fluid) and different capillary numbers (Ca), where

$$M = \frac{\mu^{nw}}{\mu^{w}}, \quad (1)$$

$$Ca = \frac{\mu^{nw} q}{\sigma^{wn}}. \quad (2)$$

Here, μ^{nw} and μ^w are the dynamic viscosities of the non-wetting and wetting phase (Pa s) respectively. σ^{wn} is the interfacial tension between the non-wetting and wetting phase (N/m) and q is the Darcy velocity (m/s) in the experiments. They categorize primary drainage processes into three distinguished regimes, known through the shape of the displacement front, based on the combination of the viscosity ratio and the Ca number. In a water-PDMS-Fluorinert system, where Fluorinert (Section 2) is the wetting phase and water is the non-wetting one, the viscosity ratio between the invading and the defending fluid during a drainage process is $M = 0.21$ ($\log M = -0.7$). In a glass porous medium,

Table 1
Image acquisition settings.

	Volumetric flux ($\mu\text{l}/\text{min}$)	Ca (–)	Image acquisition rate (fps)	Number of processed images	Image size (Pixels)
Exp. 1	0.18	10^{-7}	1	3453	2141×1266
Exp. 2	1.8	10^{-6}	5	3468	2171×1271
Exp. 3	18	10^{-5}	20	3415	2173×1271
Exp. 4	18	10^{-5}	20	3543	2424×1416

Exp. 3 and Exp. 4 are carried out for 12 and 24 displacement events, respectively.

however, the wetting properties are inverse, meaning that in a water-glass-Fluorinert system, water is the wetting phase. In Lenormand's phase diagram, one can see that reversing the viscosity ratio can affect the displacement regime. Hence, we are putting our hypothesis of a unique surface for all data points of saturation, capillary pressure, and specific interfacial area for connected clusters to the test for a precisely-defined geometry in a hydrophobic microfluidic cell and for both drainage and imbibition.

A set of flow-controlled microfluidic experiments consisting of six drainage and six imbibition events are carried out. Images from the displacement processes are recorded at fixed time intervals. The images are processed with an in-house developed tool based on **MATLAB®** (2019), and the desired parameters, such as saturation, capillary pressure, and interfacial area, are extracted. Then, Eq. (3) is employed to fit the data points from all terminal menisci between the wetting and non-wetting phases for all displacement processes.

$$a^{wn} = \alpha (s^{inv})^\beta (1 - s^{inv})^\gamma \left(\frac{p_{REV}^c}{p^{atm}} \right)^\delta, \quad (3)$$

where a^{wn} is the specific interfacial area ($1/\text{m}$), defined as the total interfacial area of all wetting/non-wetting interfaces normalized over the bulk volume of the porous medium, s^{inv} is the saturation of the invading fluid (non-wetting during drainage and wetting during imbibition), and p_{REV}^c is the REV-scale capillary pressure. p^{atm} is the atmospheric pressure, assumed as constant in all experiments (10^5 Pa). Parameter α has units of $1/\text{m}$, and parameters β , γ and δ are dimensionless.

Further, the same fitting process is applied to the same dataset for the percolating phases only. Comparing the two fits, through R^2 (the coefficient of determination), shows how significant the consideration of only the percolating saturation of a phase is in the attempt to uniquely model capillary pressure hysteresis. We also observe a linear relationship between the saturation and the interfacial area in percolating clusters. We show that this relationship is persistent, characteristic of flow rates, and independent of the number of displacement events.

The highly temporally- and spatially-resolved microfluidic experiments and their results, presented here, are complementary to the investigations published in Vahid Dastjerdi et al. (2022a). Through these results, we are able to complete our studies for a broader range of boundary conditions (displacement types, flow rates, viscosity ratios, and geometrical factors). We show that a combination of two continuum theories (theories from Hassanizadeh and Gray (1990) and Hilfer (2006a)) has less dependency on the boundary conditions in comparison to each theory alone (displacement types, flow rates, or viscosity ratios), clearly and concisely.

2. Materials and methods

The experimental methods are similar to the ones described in Vahid Dastjerdi et al. (2022a). Minor differences are explained in the following sections:

2.1. Experimental setup

The experimental setup consists of a customized optical microscope, a microfluidic cell, and a syringe pump. Apart from the microfluidic cell and the visualization settings, the rest of the setup is similar to the one used in Vahid Dastjerdi et al. (2022a). In the following, the varying characteristics of the setup are presented.

2.1.1. Microfluidic cell

A micromodel made of PDMS with cylindrical pillars serves as the porous medium in microfluidic experiments. PDMS micromodels are widely used in microfluidic experiments since they are flexibly producible by photo- and soft lithography (Xia and Whitesides, 1998; Karadimitriou et al., 2013). In this work, the depth of the cell is $55 \mu\text{m}$, and its pore size distribution varies between $75 \mu\text{m}$ and $250 \mu\text{m}$ with a mean size of $180 \mu\text{m}$. The CAD design of the cell is available in Vahid Dastjerdi et al. (2022b). The total pore volume of the cell is $\sim 3.7 \mu\text{l}$, with a porosity of $\sim 50\%$. The channels' cross-section is very close to perfect rectangles.

2.1.2. Visualization

A Basler© acA2440-20gm monochrome camera is used in this work with a sensor size of 5 Mpx and an acquisition rate ranging from 0.07 to 23 fps. A 1 W LED light source emitting at 590 nm mounted on an F/3.2 - 135 mm Canon objective lens serves as the collimated illumination of the microscope. The light is then redirected and collected through an Edmund Optics© prism and a Sigma© F/1.8 - 135 mm tele-lens towards the camera. The region of interest is cut out from the full sensor size (2448×2050) for further processing. The visualization as well as the acquisition properties of the experiments, such as image acquisition rates and image size, are listed in Table 1. The spatial resolution in the experiments is $\sim 9.1 \mu\text{m}/\text{pixel}$. A detailed sketch of the setup can be found in Vahid Dastjerdi et al. (2022a).

2.2. Two-phase flow experiments

The wetting and the non-wetting phases are Fluorinert (3M Fluorinert™FC-43 Liquid, viscosity $4.71 \text{ Pa}\cdot\text{s}$, density $1860 \text{ kg}/\text{m}^3$) and water (viscosity $1 \text{ Pa}\cdot\text{s}$, density $997 \text{ kg}/\text{m}^3$) respectively. Since the two fluids are colorless, water is dyed with a water-soluble ink (Talens Ecoline 578 Liquid Watercolor) at a concentration of 50%. The experiments are flow-controlled, and the volumetric flux is chosen to maintain the desired Ca numbers for primary drainage. The Ca numbers are 10^{-5} , 10^{-6} , and 10^{-7} and this is achieved through volumetric fluxes of $0.18 \mu\text{l}/\text{min}$, $1.8 \mu\text{l}/\text{min}$, and $18 \mu\text{l}/\text{min}$ as listed in Table 1.

Starting with primary drainage (micromodel initially fully saturated with Fluorinert), twelve sequential displacement processes of drainage and imbibition are performed in the micromodel, by injecting $18 \mu\text{l}$ of each fluid into the microfluidic cell. The volume of the fluids is chosen to be large enough (ca. five times the pore volume) to establish a steady-state flow after the breakthrough of the injected fluid. Both fluids are injected from one side of the cell through an inlet tube, which is filled with fluid pulses before being connected to the micromodel (Fig. 1). The twelve displacement processes (primary drainage, main imbibition, and ten scanning curves) are imaged at fixed time intervals, as listed in Table 1. Moreover, the inlet pressure is logged, while having a constant head of a water column of $\sim 10 \text{ cm}$ ($\sim 1 \text{ kPa}$) at the outlet, as a back-pressure. The experiment with the largest Ca number ($\text{Ca} = 10^{-5}$) has been carried out twice (Experiments 3 and 4), once with twelve displacement events and once with twenty-four, to investigate the role of system history on the variables investigated in this work.

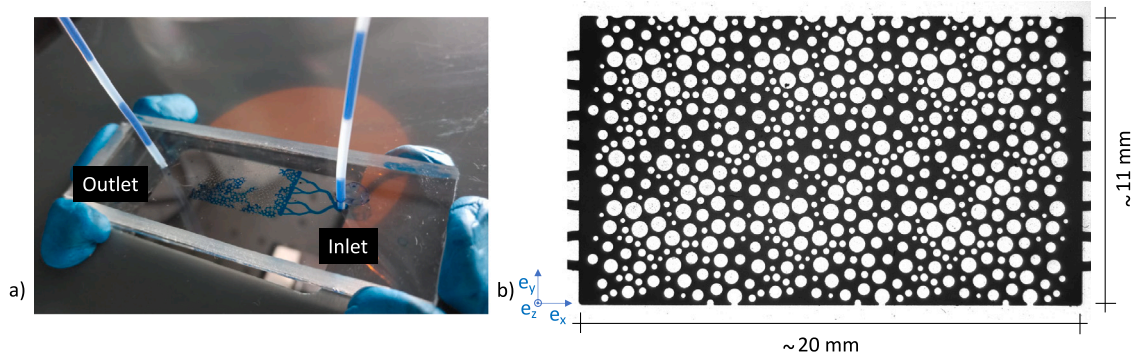


Fig. 1. (a) Microfluidic cell made of PDMS and inlet/outlet tubes with the fluids pulses inside them (blue is dyed water and transparent is Fluorinert), (b) Pore space saturated with water/ink (Under microscope with resolution of $\sim 9.1 \mu\text{m}/\text{pixel}$).

2.3. Image processing

Details about image processing can be found in Vahid Dastjerdi et al. (2022a). The main difference between the two procedures (image processing in the current work and in Vahid Dastjerdi et al. (2022a)) is the mask used for segmentation. As mentioned in 2.2, the PDMS microfluidic cell is first saturated with Fluorinert which is transparent, similar to the solid phase. Thus, segmenting the image into three phases is done with a mask, where the pore space in an image from a fully saturated cell is colored and separated from the solid skeleton.

The REV size in the investigations is calculated as the smallest volume, above which, any changes in the average value of the considered parameter are negligible. We investigate the REV size for porosity, interfacial area, and mean curvature. The domain size, which is an REV for all these parameters is in the order of 1120×1120 pixels ($\sim 10 \text{ mm} \times 10 \text{ mm}$). As the imaged porous domain in our experiments is ca. 2150×1300 pixels ($\sim 11 \text{ mm} \times 20 \text{ mm}$), the middle part of the micromodel qualifies as at least one REV.

2.4. Post-processing

Proceeding with the image processing techniques, which yield parameters such as length, curvature, and contact angle of each interface, REV-scale parameters such as saturation, total interfacial area, and average capillary pressure, are computed. Eqs. (4) to (6) are employed to calculate the interfacial area of an interface i (A_i^{wn}), the local capillary pressure based on the three-dimensional Young–Laplace equation (p_i^c), and the macroscale capillary pressure (p_{REV}^c).

$$A_i^{wn} = \frac{L_i d}{\cos \alpha} \left(\frac{\pi}{2} - \alpha \right), \quad (4)$$

where L_i is the length of interface i (m), α is the contact angle in e_z direction (56° during drainage and 58° during imbibition), and d is the depth of the cell ($55 \mu\text{m}$). The collective interfacial area of all interfaces in one image is the REV-scale interfacial area associated with one image.

$$p_i^c = \sigma^{wn} \left(\kappa_i + 2 \frac{\cos \alpha}{d} \right), \quad (5)$$

where p_i^c is the local capillary pressure at interface i , σ^{wn} is the surface tension between Fluorinert and water, which is equal to $55 \text{ mN}/\text{m}^2$, κ_i is the curvature of each interface in the $e_x \times e_y$ plane ($1/\text{m}$). The contact angle α in the $e_y \times e_z$ direction is assumed to be equal to the mean value of the contact angles calculated in the $e_x \times e_y$ plane for all interfaces (Fig. 1). Averaging the local capillary pressures over the interfacial area (Eq. (6)) delivers the macroscale (REV) capillary pressure

$$p_{REV}^c = \frac{\sum (p_i^c A_i^{wn})}{\sum A_i^{wn}}, \quad (6)$$

where A_i^{wn} is the area of interface i (m^2).

Triplets of data containing the saturation of the invading phase, the total specific area of the wetting/non-wetting interfaces, and the REV-scaled capillary pressure are formed for all clusters in the porous domain during flow. The same procedure is carried out to extract the data for only the flowing clusters. To quantify the affiliation of the data point with a single surface, as we hypothesize, a function as Eq. (3) is used to fit the data. The goodness of fit in the form of R^2 is presented in Section 3.

3. Results

The first step in our investigations is to ensure that the PDMS micromodels serve the purpose of this study, for which we need to determine the connectivity of the clusters to the flow precisely. To ensure the compatibility of the cell, we observe the volume of several clusters (detected as disconnected from the images) for both phases during drainage and imbibition. If a significant change is detected in their volume, a connection that is not detectable with our image processing procedure (for example, through corner flow) can be assumed. If the volume of a cluster, which visually looks disconnected from its neighbors, does not change during flow, it is considered an isolated cluster. In Fig. 2, four wetting phase clusters are marked with red circles at different locations. The images show the configuration of phase clusters in the micromodel at the end of a drainage event (Fig. 2a) and an imbibition event (Fig. 2b). The volume change of the four clusters during those drainage and imbibition events is studied. Since their volume changes only by 0.2% to 0.7%, we assume the clusters are disconnected. The same analysis is carried out for the non-wetting clusters, and as expected, the volume change is in the order of the processing error. Given the above, the connectivity of wetting and non-wetting clusters (at the scales relevant to this work) is detectable from the images. Thus, the recorded images during both imbibition and drainage are processed, and the derived quantities are analyzed and presented in the following.

With the use of the image processing procedures described in Vahid Dastjerdi et al. (2022a), specific interfacial area, capillary pressure, and saturation are calculated for each image, initially for all clusters and then only for the connected ones. Plots of specific interfacial area versus saturation gathered from the experiments are shown in Figs. 3a and 3b for all clusters and connected clusters, respectively. Similarly, Figs. 3c and 3d show the capillary pressure-saturation data pairs from all clusters and connected clusters, respectively. It is evident that the data for connected clusters show better-behaving trends.

The apparent linear dependency of the specific interfacial area on the saturation for the connected clusters, the increase in the slope of this linear dependency, and the reduction in the variability motivate us to look into their relationship more thoroughly. In Fig. 4, this relation is investigated in the experiment with Ca equal to 10^{-5} and for drainage and imbibition separately. During primary drainage, the

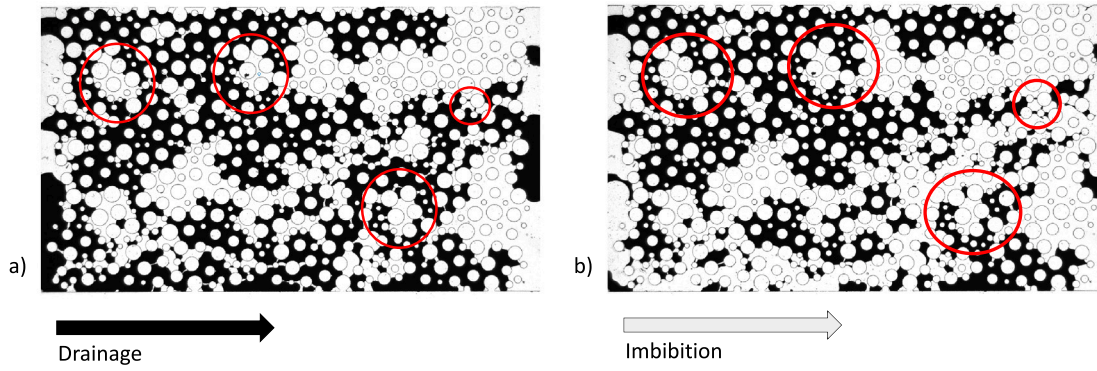


Fig. 2. Four disconnected wetting phase clusters, where the volume is observed during (a) Drainage and (b) Imbibition. The wetting phase (Fluorinert) is recorded as white, and the non-wetting phase (dyed water) is recorded as black.

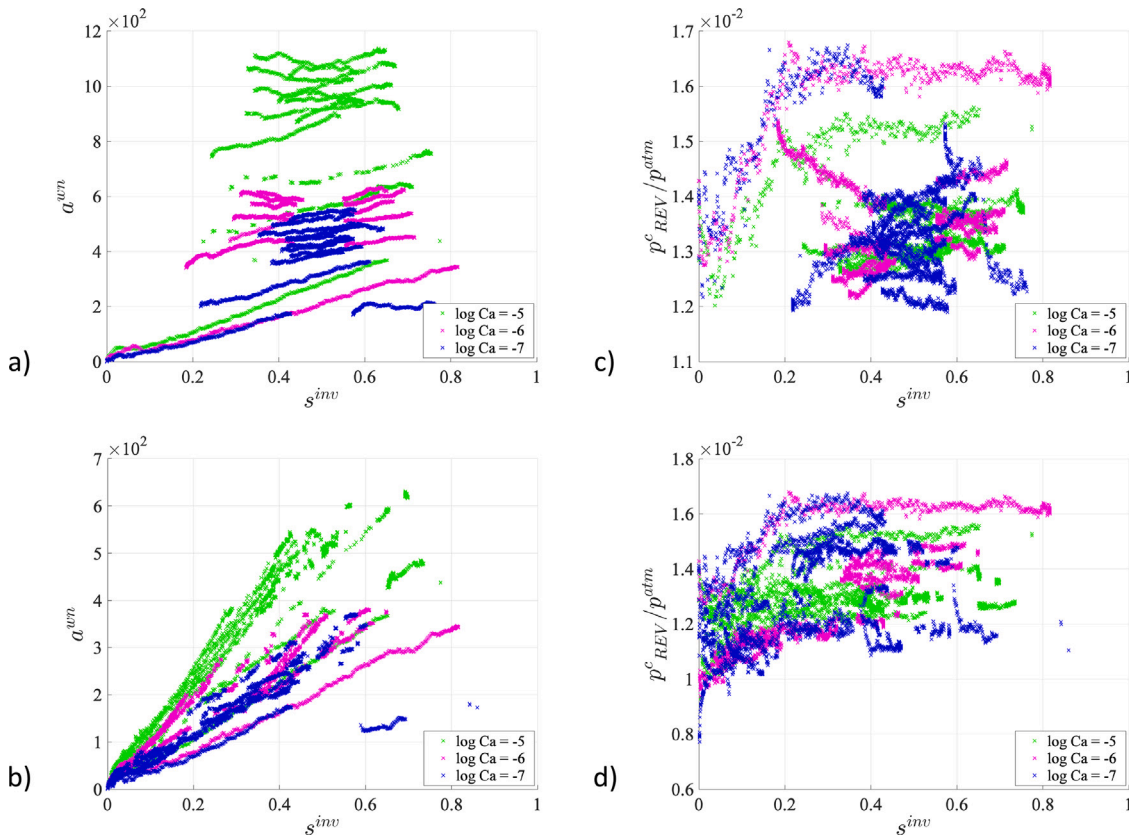


Fig. 3. Data gathered from the experiments by image processing: (a) Specific interfacial area for all clusters, (b) Specific interfacial area for connected clusters, (c) Normalized capillary pressure for all clusters, (d) Normalized capillary pressure for connected clusters.

specific interfacial area grows linearly with saturation with a slope of 675 (l/m). However, the slope increases as the experiment evolves and reaches 1540 (l/m) for the eleventh scanning curve. For imbibition, the corresponding slope steadily increases from the minimum value of 610 (l/m) for the main imbibition to the maximum value of 1370 (l/m) for the last imbibition process. In addition, it is noteworthy that the difference between the two processes reduces as the number of displacements (history of the system) increases. Observations of the other two experiments also reveal the same pattern: the slope is always between 230 (l/m) to 1540 (l/m), with the lowest value being associated with the main imbibition of the slowest experiment ($Ca = 10^{-7}$) and the highest value corresponding to the last drainage of the fastest experiment ($Ca = 10^{-5}$).

The slope of the fitted line for connected clusters seems to stop increasing after some scanning events, resulting in a unique domain

that accommodates all the specific interfacial area values. To verify this hypothesis, the experiment with the Ca number 10^{-5} is repeated with 24 cycles instead of 12. In Fig. 5, one can see the specific interfacial area generated between the wetting and the non-wetting phase for clusters connected to the inlet during both sets of experiments. Thus, the domain of the set of state variables (a^{wn}, s) seems to be well-defined for a single Ca number and a given porous medium. With this second experiment, we also investigate the dependence of the interfacial area on the pore structure in an experiment where the capillary forces are not dominant. The Ca numbers for the experiments are chosen so that a transition between capillary fingering and viscous fingering is expected (based on Lenormand's phase diagram). Our results show that even in an experiment that is not fully capillary dominated ($\log(Ca) = -5$ and $\log(M) = -0.7$), the generation of interfacial area is the same as long as the porous medium stays the same. We also observe that the more

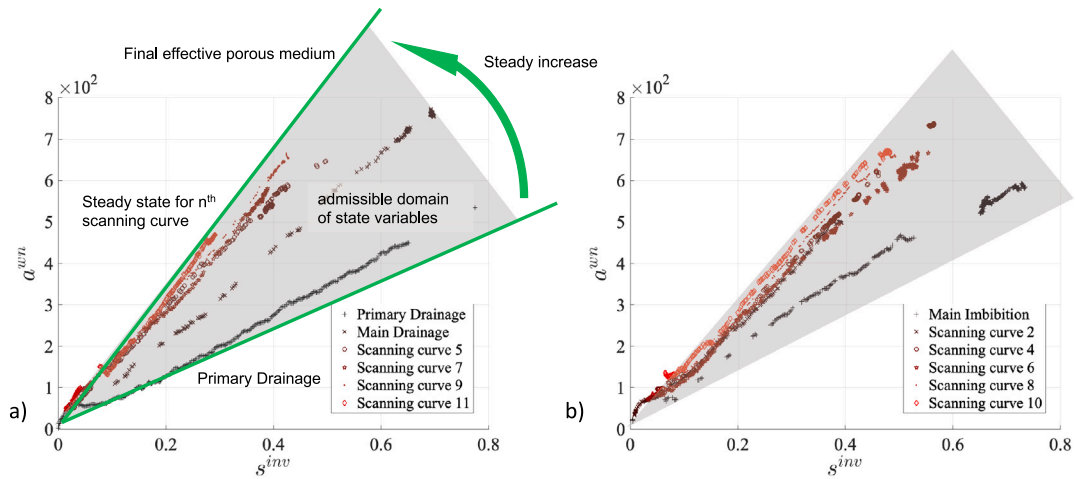


Fig. 4. The linear pattern of the specific interfacial area versus saturation for connected clusters (a) Drainage, (b) Imbibition; Experiment 3, $Ca = 10^{-5}$.

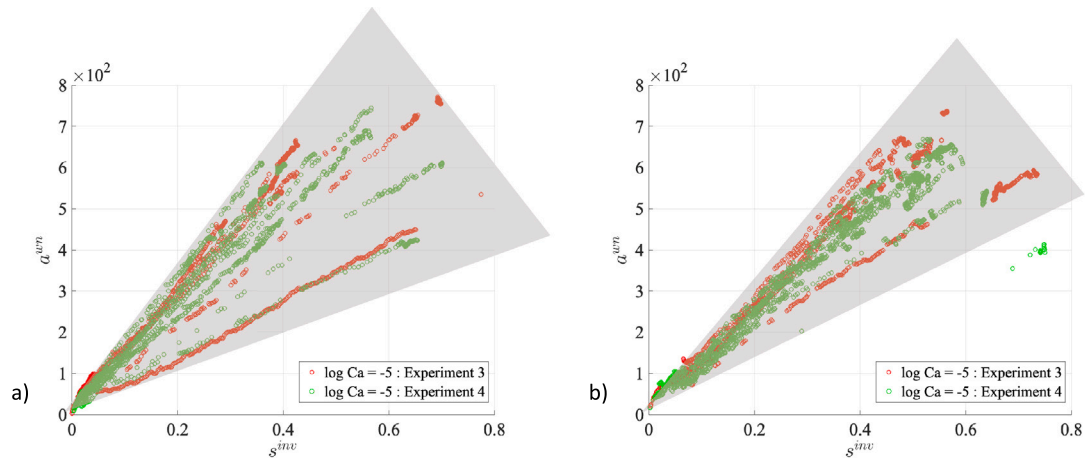


Fig. 5. The linear pattern of the specific interfacial area versus saturation for connected clusters in two experiments (one with 12 events and the second with 24 events) with the same Ca number (10^{-5}) (a) Drainage, (b) Imbibition.

displacement events happen in the microfluidic cell, the less the change in the produced interfacial area is, which implies the formation of preferential flow paths after some cycles. The formation of preferential paths could be interpreted as forming an effective porous medium, slightly different during drainage and imbibition events. Although the displacement events are executed 24 times in the second trial with $Ca = 10^{-5}$, the specific interfacial area stays in the range of the first trial. Investigating this observation in other case studies can help us estimate the $s - a^{wn}$ curves in various phenomena, where the displacement events happen repeatedly (Fig. 6). Examples are the cyclic wetting and drying of soil (Zhao et al., 2018), fluids displacement in fuel cells (Andersson et al., 2016; Niblett et al., 2020), Subsurface storage of compressed air (CAES) (Zhang et al., 2020) or hydrogen (Tarkowski, 2019).

Following the procedure described in Section 1, Eq. (3) is fitted to the data point triplets from one displacement process. This work's main interest is finding the state variables of a two-phase porous medium flow independent of the viscosity ratio of the fluids, the displacement process (drainage or imbibition), and the Ca number. Putting all the data points from drainage and imbibition during one experiment together serves the purpose of studying our hypothesis on the type of displacement process. Moreover, the results from analyzing the combination of the data from the experiments with various Ca numbers indicate the dependency of the hypothesis on the Ca number. In other words, the data from experiments with Ca numbers 10^{-7} and

10^{-6} are combined, and the same fitting process is applied. Similarly, combinations of the experiments with Ca numbers 10^{-6} and 10^{-5} , as well as the experiments with Ca numbers 10^{-7} , 10^{-6} , and 10^{-5} are studied. The experiment with Ca number 10^{-5} is chosen as an example, and the goodness of fit in the form of R^2 is presented in Table 2. The experiment with the capillary number of 10^{-5} is chosen as a more representative example since a significant viscous contribution to the flow regime is expected. Thus, there is a larger number of disconnections, and, consecutively, increasing the probability of establishing preferential flow paths for fewer cyclic events. The R^2 values illustrate the nearly perfect fitting of Eq. (3) to the single displacement processes when only the clusters connected to the flow are accounted for. The R^2 values in the last row of Table 2 show how much the fitting is improved for connected clusters for a dataset containing drainage and imbibition displacements.

The effect of Ca number on the fitting is presented in Table 3. The R^2 values listed in Table 3 make it clear that the fitting improves when only the data from connected clusters are considered. This is especially of interest for the most transient experiment, where the fitting for all clusters is bad. The better fit in the case of connected clusters supports the hypothesis that connectedness and specific interfacial area should both be involved in theories related to two-phase flow. Furthermore, a glance at the results presented in Vahid Dastjerdi et al. (2022a) for a viscosity ratio of 0.21 (See Table 4) is an indication of the validity of the theory independent of the viscosity ratio. Comparing Tables 3

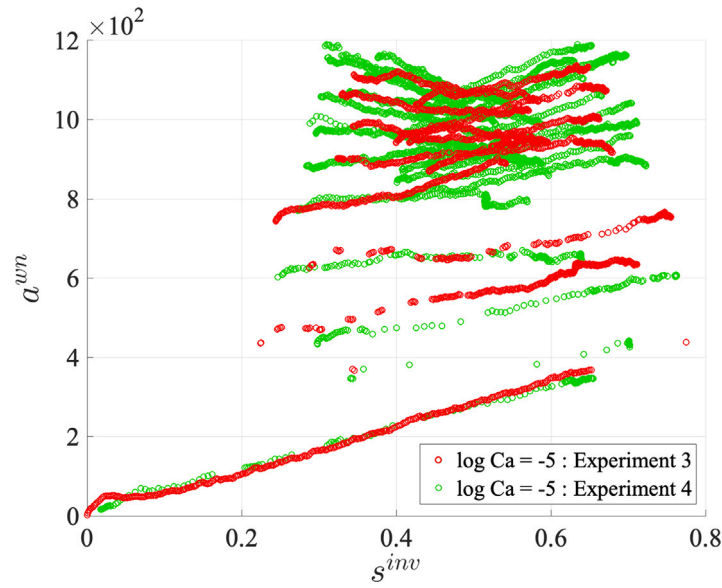


Fig. 6. The specific interfacial area versus saturation in two experiments (one with 12 events and the second with 24 events) with the same Ca number (10^{-5}) for all clusters.

Table 2

Goodness of fit (R^2) for drainage-imbibition processes from the experiment with Ca number 10^{-5} .

	All clusters included	Connected clusters
Primary drainage	0.993	0.993
Main imbibition	0.94	0.998
Scanning curve	0.97	0.998
Scanning curve	0.98	1
Scanning curve	0.97	1
Scanning curve	0.93	1
Scanning curve	0.97	1
Scanning curve	0.87	1
Scanning curve	0.98	1
Scanning curve	0.96	1
Scanning curve	0.97	0.999
Scanning curve	0.92	0.996
All data points ^a	0.57	0.87

^aAccumulated data points from all twelve displacements in the experiment.

and 4, one can see that the fit improves for the connected clusters in comparison to all clusters for both viscosity ratios of 4.7 and 0.21. In addition to the Ca number, viscosity ratio, and displacement process, there is evidence (in our results) that this hypothesis holds for various geometries. The evidence comes from the fact that the hypothesis is consistent in two relatively different geometries, as the geometry (the pore throat/pore depth ratio and shape of the channels) of the PDMS cell used in this study is different from the glass micromodel used in Vahid Dastjerdi et al. (2022a). However, the effects of the geometry on the fitting parameters must be addressed thoroughly in future research.

As described in Section 1, in this work, the existence of a single surface for $P^c - s - a^{wn}$ is investigated. In particular, we have fitted Eq. (3) to various datasets (with different Ca numbers) and/or their combinations and have obtained values for the parameters α , β , γ , and δ . The resulting equations for all clusters and connected clusters are given in Eqs. (7) and (8), respectively. These equations are formed by substituting the values of parameters α , β , γ , and δ as calculated for all data from the three experiments in Eq. (3).

$$a^{wn} = 0.034 (s^{inv})^{1.11} (1 - s^{inv})^{0.485} \left(\frac{P^c_{REV}}{P^{atm}} \right)^{-2.53}, \quad (7)$$

$$a^{wn} = 14.53 (s^{inv})^{1.17} (1 - s^{inv})^{0.38} \left(\frac{P^c_{REV}}{P^{atm}} \right)^{-1}. \quad (8)$$

We use these equations to calculate specific interfacial area for all experimentally measured values of saturation and capillary pressure, and compare the calculated values with the corresponding measured values of specific interfacial area in Fig. 7. It can be clearly seen that Eq. (8) (for connected clusters only) does a better job in predicting measured values of specific interfacial area than Eq. (7) (for all clusters). Note that the data from the three experiments are not distributed in the same pattern. One can see that the experiments with Ca numbers 10^{-6} and 10^{-7} are better-captured by Eq. (8) than the experiment with Ca number 10^{-5} . This could again be associated with the growing viscous effects in the experiments and the corresponding pore-scale velocity fields.

4. Discussion and conclusion

The linear relation between the saturation of the invading fluid and the specific interfacial area is characteristic of almost all displacement regimes. The data points include pairs of specific interfacial area and saturation from four experiments, two of which (with Ca numbers 10^{-7} and 10^{-6}) seem to be in the capillary regime (based on the work from Lenormand et al. (1988)) and fall on top of each other. The other two experiments (with Ca number 10^{-5}) are also similar, regardless of the number of displacement events (Fig. 6). These observations imply that the specific interfacial area associated with the connected clusters in a porous medium fall within a domain boundary by two straight lines, one corresponding to the main imbibition and the other to the last scanning drainage event. One can see in Fig. 5, that the rate of change of the specific interfacial area vs. saturation in the clusters connected to the inlet stays almost constant after the main events (main drainage and main imbibition). This is regardless of the number of displacement events and happens for both experiments 3 and 4. Moreover, in some processes, the re-connection of some disconnected clusters causes discontinuities in the data points. However, the slope of the linear relation of the specific interfacial area, and saturation is preserved (see main drainage in Fig. 4a or main imbibition in Fig. 4b).

Moreover, with the results presented here, we show that the description of a two-phase system can be drastically improved from a continuum perspective when specific interfacial area and, at the same time, discrimination between connected and disconnected clusters are considered. For a range of Ca numbers, all triplet data points of saturation, capillary pressure, and interfacial area can be fitted with a surface. Although, for increasing boundary flux conditions, considering

Table 3Goodness of fit (R^2) for accumulative data in single experiments and their combinations for viscosity ratio 4.7.

		Log(Ca)					
		-7	-6	-5	-7 and -6	-6 and -5	-7 and -6 and -5
R^2	All clusters	0.82	0.88	0.57	0.58	0.51	0.33
	Connected clusters	0.82	0.92	0.87	0.82	0.76	0.70

Table 4Goodness of fit (R^2) for accumulative data in single experiments and their combinations for viscosity ratio 0.21 (Vahid Dastjerdi et al., 2022a).

		Log(Ca)					
		-7	-6	-5	-7 and -6	-6 and -5	-7 and -6 and -5
R^2	All clusters	0.67	0.79	0.74	0.66	0.72	0.48
	Connected clusters	0.94	0.86	0.86	0.90	0.74	0.70

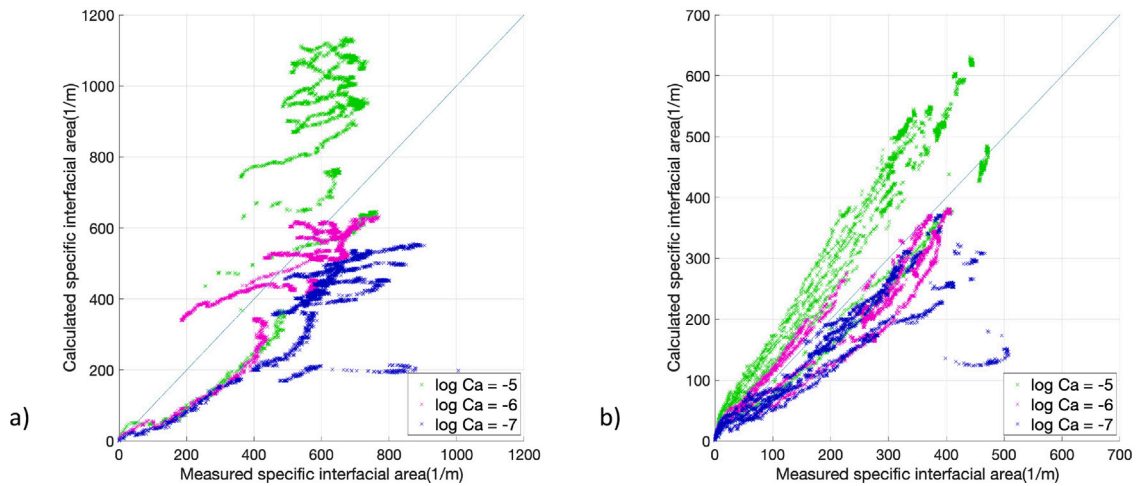


Fig. 7. Correlation between the calculated specific interfacial area and the measured specific interfacial area from the experiments: (a) Using Eq. (7) for all clusters, (b) Using Eq. (8) for connected clusters.

only the interfacial area seems to reach a conceptual limitation (See R^2 values for all clusters in Table 3), the R^2 values for connected clusters show a much smaller dependency on flow rates.

There is, however, a strong deviation from an ideal fitting when combining various Ca numbers. Thus, to be able to find a single description for two-phase flow that fits all boundary conditions, additional parameters, or even state variables are needed. Nevertheless, there is an essential improvement in the fitting when in addition to interfacial area the connectivity of the phases is also considered. The R^2 increases from 0.33 to 0.70 (still not ideal), when all experiments are analyzed as one dataset (Table 3). Given the results of this work, the logical next step would be to evaluate our proposed combination of two continuum-scale theories for the effect of the geometrical factors. This includes the investigation on the pore scale of how local constrictions favor, or not, disconnections due to the interplay between capillary and viscous forces. Thus, further research with a variety of pore-scale geometries, and also the corresponding pore and throat size distributions, as well as the networks' correlation lengths and coordination factors should be carried out.

In correlation to the work from Vahid Dastjerdi et al. (2022a), we need to emphasize the cross-sectional shape's comparative effect on flow evolution, mainly regarding the connectivity of the wetting phase. The channel properties of the PDMS microfluidic cell and its wetting properties restrict the connection of the wetting phase, and thus, allow for the inclusion of imbibition in the results, without any biasing. The addition of imbibition allows us to create a dataset that represents better a real-life situation or, even better, a more realistic displacement scenario in terms of case completeness. Moreover, in the case of PDMS, where a rectangular cross-sectional shape can safely

be assumed, there is an increased certainty in how the contact angle is calculated and accounted for, especially for the in-plane direction, which is not optically visible. The experiments in the PDMS cell make it even possible to emphasize more the potential effect of the pore scale geometry and its correlation to an increasing deviation of the proposed fitting function for combining Ca numbers, as manifested in Tables 3 and 4.

5. Research data

The datasets are available in the Data Repository of the University of Stuttgart (DaRUS). The datasets (Vahid Dastjerdi et al., 2022b) provide images of optical microscopy (*.tif) together with the pressure data (*.csv). Moreover, the CAD design of the microfluidic cell is available.

CRediT authorship contribution statement

Samaneh Vahid Dastjerdi: Conceptualization, Methodology, Software, Validation, Formal analysis, Investigation, Resources, Data curation, Writing – original draft, Visualisation. **Nikolaos Karadimitriou:** Conceptualization, Methodology, Formal analysis, Investigation, Resources, Data curation, Writing – original draft. **S. Majid Hasanizadeh:** Conceptualization, Formal analysis, Writing – review & editing, Supervision. **Holger Steeb:** Conceptualization, Formal analysis, Writing – review & editing, Supervision, Project administration, Funding acquisition.

Declaration of competing interest

The authors declare that they have no known competing financial interests or personal relationships that could have appeared to influence the work reported in this paper.

Data availability

The data has been published on the Depository of University of Stuttgart. The link is provided in the article.

Acknowledgments

This work is funded by Deutsche Forschungsgemeinschaft (DFG, German Research Foundation) under Germany's Excellence Strategy - EXC 2075 – 390740016. We acknowledge the support by the Stuttgart Center for Simulation Science (SimTech). HS and NK would like to thank the Deutsche Forschungsgemeinschaft (DFG, German Research Foundation) for supporting this work by funding SFB 1313, Project Number 327154368.

References

- Abdelkareem, M.A., Elsaid, K., Wilberforce, T., Kamil, M., Sayed, E.T., Olabi, A., 2021. Environmental aspects of fuel cells: A review. *Sci. Total Environ.* 752, 141803.
- Alvarado, V., Manrique, E., 2010. Enhanced Oil Recovery Concepts. Gulf Professional Publishing, pp. 7–16.
- Andersson, M., Beale, S., Espinoza, M., Wu, Z., Lehnert, W., 2016. A review of cell-scale multiphase flow modeling, including water management, in polymer electrolyte fuel cells. *Appl. Energy* 180, 757–778.
- Armstrong, R.T., Porter, M.L., Wildenschild, D., 2012. Linking pore-scale interfacial curvature to column-scale capillary pressure. *Adv. Water Resour.* 46, 55–62.
- Brooks, R.H., Corey, A.T., 1964. Hydraulic properties of porous media.
- Cheng, J.T., Pyrak-Nolte, L.J., Nolte, D.D., Giordano, N.J., 2004. Linking pressure and saturation through interfacial areas in porous media. *Geophys. Res. Lett.* 31, L08502.
- Choudhury, K., Saha, D., Chakraborty, P., 2001. Geophysical study for saline water intrusion in a coastal alluvial terrain. *J. Appl. Geophys.* 46 (3), 189–200.
- Doster, F., Hilfer, R., 2014. A comparison between simulation and experiment for hysteretic phenomena during two-phase immiscible displacement. *Water Resour. Res.* 50, 681–686.
- Hassanizadeh, S.M., Gray, W.G., 1990. Mechanics and thermodynamics of multiphase flow in porous media including interphase boundaries. *Adv. Water Resour.* 13, 169–186.
- Hassanizadeh, S.M., Gray, W.G., 1993. Thermodynamic basis of capillary pressure in porous media. *Water Resour. Res.* 29, 3389–3405.
- Held, R.J., Celia, M.A., 2001. Modeling support of functional relationships between capillary pressure, saturation, interfacial area and common lines. *Adv. Water Resour.* 24, 325–343.
- Herring, A.L., Harper, E.J., Andersson, L., Sheppard, A., Bay, B.K., Wildenschild, D., 2013. Effect of fluid topology on residual nonwetting phase trapping: Implications for geologic CO₂ sequestration. *Adv. Water Resour.* 62, 47–58.
- Herring, A.L., Middleton, J., Walsh, R., Kingston, A., Sheppard, A., 2017. Flow rate impacts on capillary pressure and interface curvature of connected and disconnected fluid phases during multiphase flow in sandstone. *Adv. Water Resour.* 107, 460–469.
- Hilfer, R., 2006a. Capillary pressure, hysteresis and residual saturation in porous media. *Phys. A* 359, 119–128.
- Hilfer, R., 2006b. Macroscopic capillarity and hysteresis for flow in porous media. *Phys. Rev. E* 73, 016307.
- Hilfer, R., Armstrong, R.T., Berg, S., Georgiadis, A., Ott, H., 2015. Capillary saturation and desaturation. *Phys. Rev. E* 92, 063023.
- Hilfer, R., Doster, F., 2010. Percolation as a basic concept for macroscopic capillarity. *Transp. Porous Media* 82, 507–519.
- Joekar-Niasar, V., Hassanizadeh, S.M., 2011. Specific interfacial area: The missing state variable in two-phase flow equations? *Water Resour. Res.* 47, W05513.
- Joekar-Niasar, V., Hassanizadeh, S.M., Leijnse, A., 2008. Insights into the relationships among capillary pressure, saturation, interfacial area and relative permeability using pore-network modeling. *Transp. Porous Media* 74, 201–219.
- Karadimitriou, N.K., Hassanizadeh, S.M., Joekar-Niasar, V., Kleingeld, P., 2014. Micro-model study of two-phase flow under transient conditions: Quantifying effects of specific interfacial area. *Water Resour. Res.* 50, 8125–8140.
- Karadimitriou, N.K., Musterd, M., Kleingeld, P.J., Kreutzer, M.T., Hassanizadeh, S.M., Joekar-Niasar, V., 2013. On the fabrication of PDMS micromodels by rapid prototyping, and their use in two-phase flow studies. *Water Resour. Res.* 49, 2056–2067.
- Khorsandi, S., Li, L., Johns, R.T., 2021. A new way of compositional simulation without phase labeling. *SPE Journal* 26, 940–958.
- Land, C.S., 1968. Calculation of imbibition relative permeability for two- and three-phase flow from rock properties. *Soc. Petroleum Eng. J.* 8, 149–156.
- Lenormand, R., Touboul, E., Zarcone, C., 1988. Numerical models and experiments on immiscible displacements in porous media. *J. Fluid Mech.* 189, 165–187.
- Leverett, M., 1941. Capillary behavior in porous solids. *Trans. AIME* 142 (01), 152–169.
- Lipiec, J., Kuś, J., Słowińska-Jurkiewicz, A., Nosalewicz, A., 2006. Soil porosity and water infiltration as influenced by tillage methods. *Soil Tillage Res.* 89 (2), 210–220.
- MATLAB®, 2019. MATLAB Version 9.6.0.1214997 (R2019b). The MathWorks, Inc., Natick, Massachusetts.
- McClure, J.E., Ramstad, T., Li, Z., Armstrong, R.T., Berg, S., 2020. Modeling geometric state for fluids in porous media: Evolution of the Euler characteristic. *Transp. Porous Media* 133, 229–250.
- Miller, C.T., Bruning, K., Talbot, C.L., McClure, J.E., Gray, W.G., 2019. Nonhysteretic capillary pressure in two-fluid porous medium systems: Definition, evaluation, validation, and dynamics. *Water Resour. Res.* 55, 6825–6849.
- Muggeridge, A., Cockin, A., Webb, K., Frampton, H., Collins, I., Moulds, T., Salino, P., 2014. Recovery rates, enhanced oil recovery and technological limits. *Philos. Trans. R. Soc. Lond. Ser. A Math. Phys. Eng. Sci.* 372, 20120320.
- Niblett, D., Mularczyk, A., Niasar, V., Eller, J., Holmes, S., 2020. Two-phase flow dynamics in a gas diffusion layer - gas channel - microporous layer system. *J. Power Sources* 471, 228427.
- Niessner, J., Hassanizadeh, S.M., 2008. A model for two-phase flow in porous media including fluid-fluid interfacial area. *Water Resour. Res.* 44 (8), 006721.
- Osei-Bonsu, K., Khorsandi, S., Piri, M., 2020. Quantitative analysis of phase topology evolution during three-phase displacements in porous media. *Lab Chip* 20, 2495–2509.
- Parr, J., Bertrand, A., 1960. Water infiltration into soils. In: Normax, A. (Ed.), In: *Advances in Agronomy*, vol. 12, Academic Press, pp. 311–363.
- Porter, M.L., Schaap, M.G., Wildenschild, D., 2009. Lattice-Boltzmann simulations of the capillary pressure-saturation-interfacial area relationship for porous media. *Adv. Water Resour.* 32 (11), 1632–1640.
- Schlüter, S., Berg, S., Rücker, M., Armstrong, R.T., Vogel, H.-J., Hilfer, R., Wildenschild, D., 2016. Pore-scale displacement mechanisms as a source of hysteresis for two-phase flow in porous media. *Water Resour. Res.* 52, 2194–2205.
- Sharaf, O.Z., Orhan, M.F., 2014. An overview of fuel cell technology: Fundamentals and applications. *Renew. Sustain. Energy Rev.* 32, 810–853.
- Shokri, J., Godinez-Brizuela, O.E., Erfani, H., Chen, Y., Babaei, M., Berkowitz, B., Niasar, V., 2022. Impact of displacement direction relative to heterogeneity on averaged capillary pressure-saturation curves. *Water Resour. Res.* 58 (2), e2021WR030748.
- Tarkowski, R., 2019. Underground hydrogen storage: Characteristics and prospects. *Renew. Sustain. Energy Rev.* 105, 86–94.
- Todd, D.K., 1974. Salt-water intrusion and its control. *J. Am. Water Works Assoc.* 66 (3), 180–187.
- Vahid Dastjerdi, S., Karadimitriou, N.K., Hassanizadeh, S.M., Steeb, H., 2022a. Experimental evaluation of fluid connectivity in two-phase flow in porous media during drainage. *Water Resour. Res.* 58 (11), e2022WR033451.
- Vahid Dastjerdi, S., Karadimitriou, N., Steeb, H., 2022b. Data for: Experimental Evaluation of Connectivity in Two-phase Flow in Porous Media. DaRUS, <http://dx.doi.org/10.18419/darus-2841>.
- Van Genuchten, M., 1980. A closed-form equation for predicting the hydraulic conductivity of unsaturated soils. *Soil Sci. Am. J.* 44, 892–898.
- Xia, Y., Whitesides, G.M., 1998. Soft lithography. *Annu. Rev. Mater. Sci.* 37, 550–575.
- Zhang, J., Zhang, H., Lee, D., Ryu, S., Kim, S., 2020. Microfluidic study on the two-phase fluid flow in porous media during repetitive drainage-imbibition cycles and implications to the caes operation. *Transp. Porous Media* 131, 449–472.
- Zhao, Y., Ren, S., Jiang, D., Liu, R., Wu, J., Jiang, X., 2018. Influence of wetting-drying cycles on the pore structure and mechanical properties of mudstone from Simian Mountain. *Constr. Build. Mater.* 191, 923–931.
- Zhuang, L., Hassanizadeh, S.M., Kleingeld, P.J., van Genuchten, M., 2017. Revisiting the horizontal redistribution of water in soils: Experiments and numerical modeling. *Water Resour. Res.* 53 (9), 7576–7589.